# Numerical Simulations of Shelterbelt Effects on Wind Direction

HAO WANG AND EUGENE S. TAKLE

*Department of Geological and Atmospheric Sciences, and Department of Agronomy, Iowa State University, Ames, Iowa*

(Manuscript received 17 October 1994, in final form 7 March 1995)

ABSTRACT

A neutral boundary layer nonhydrostatic numerical model is used to determine the characteristics of shelterbelt effects on mean wind direction and to study the processes causing wind rotation when air passes through a shelterbelt. The model uses a turbulence scheme that includes prognostic equations for turbulence kinetic energy and a master length scale proposed by Mellor and Yamada. The simulated results are in quantitative agreement with Nord's field measurements. The spatial variation of wind rotation and its dependence on incident angle and shelterbelt porosity is analyzed. Dynamic processes of the wind rotation and its interactions with drag force and pressure perturbation are also discussed. It is concluded that shear of wind direction should be considered, along with shear of speed, in determining turbulent fluxes in the vicinity of a shelterbelt.

## 1. Introduction

Natural and man-made windbreaks and shelterbelts have been used for centuries for protection from the wind. More recently, agroforestry ecosystems consisting of shelterbelt and windbreak networks have been established throughout the world for increasing productivity, promoting environmental sustainability, and improving the quality of life. All functional effects of shelterbelts are directly related to modification of airflow patterns. Reviews of recent research have been given by van Eimern et al. (1964), Rosenberg (1979), McNaughton (1988), and Heisler and Dewalle (1988). Shelterbelts influence the flow field by reducing wind speed and changing wind direction. The former effect has been intensively investigated, but the latter has been studied very little.

Quantitative observation of wind direction is more difficult than the observation of wind speed, especially in wind tunnel experiments, on which most existing knowledge of shelterbelt effects is based. Only a few investigators have reported qualitative and quantitative observational differences in wind direction between sheltered and unsheltered sites (Bringmann and Kaiser 1955, cited by van Eimern et al. 1964; Nord 1991). Shelterbelt modification of microclimate depends on wind direction (van Eimern et al. 1964) because the drag force exerted by shelterbelts is strongly dependent on the wind trajectory through the barrier.

Most previous theoretical and numerical modeling work considered only the relatively simple example of a uniformly porous, artificial barrier resting on a uniform surface with wind blowing at a right angle (Kaiser 1959; Plate 1971; Taylor 1988; Counihan et al. 1974; Hagen et al. 1981; Wilson 1985, 1987; Wang and Shen 1989; Wang 1991a,b, 1992; Wang and Takle 1995). To our knowledge, there are no theoretical and numerical studies that address oblique approach flows.

In this paper, we report results of a nonhydrostatic numerical model that has been used to study the physical and dynamic processes by which a shelterbelt influences wind direction. We also present analyses of the spatial variations of changes in wind direction and the relationships of wind rotation to shelterbelt density and angle of wind incidence. This paper is the third in a series of papers (Wang and Takle 1995) that describe the aerodynamic fields around shelterbelts. The first paper discusses the details of how turbulent fields generated by the shelter interact with turbulence fields of the undisturbed boundary layer. The second gives results of simulations for winds perpendicular to the shelter.

## 2. Model

We consider an infinitely long shelterbelt on flat ground with the $z$ coordinate upward, $x$ coordinate horizontally perpendicular, and $y$ parallel to the shelterbelt. Shelterbelt height generally is about 10 m, which is less than the height of the atmospheric boundary layer, so the effect of the Coriolis force may be neglected. We limit our attention to neutral stratification for which, under the Boussinesq approximation, the nonhydrostatic, incompressible atmospheric continuity equation and equations of motion may be written as

*Corresponding author address:* Dr. Hao Wang, Department of Geological and Atmospheric Sciences, Iowa State University, 3010 Agronomy Hall, Ames, IA 50011.
E-mail: wanghao@iastate.edu

$$\frac{\partial u}{\partial x} + \frac{\partial v}{\partial y} + \frac{\partial w}{\partial z} = 0 \quad (1)$$

$$\frac{\partial u}{\partial t} = -\frac{1}{\rho}\frac{\partial p}{\partial x} - u\frac{\partial u}{\partial x} - v\frac{\partial u}{\partial y} - w\frac{\partial u}{\partial z} - \frac{\partial \overline{u'^2}}{\partial x} - \frac{\partial \overline{u'v'}}{\partial y} - \frac{\partial \overline{u'w'}}{\partial z} - C_d A U u \quad (2)$$

$$\frac{\partial v}{\partial t} = -\frac{1}{\rho}\frac{\partial p}{\partial y} - u\frac{\partial v}{\partial x} - v\frac{\partial v}{\partial y} - w\frac{\partial v}{\partial z} - \frac{\partial \overline{u'v'}}{\partial x} - \frac{\partial \overline{v'^2}}{\partial y} - \frac{\partial \overline{v'w'}}{\partial z} - C_d A U v \quad (3)$$

$$\frac{\partial w}{\partial t} = -\frac{1}{\rho}\frac{\partial p}{\partial z} - u\frac{\partial w}{\partial x} - v\frac{\partial w}{\partial y} - w\frac{\partial w}{\partial z} - \frac{\partial \overline{u'w'}}{\partial x} - \frac{\partial \overline{v'w'}}{\partial y} - \frac{\partial \overline{w'^2}}{\partial z} - C_d A U w, \quad (4)$$

where $u$, $v$, and $w$ are mean wind speed components in $x$, $y$, and $z$ direction, respectively, and $u'$, $v'$, and $w'$ are their fluctuating values. For convenience, we omit the overbar on mean values. The term $p$ is the pressure perturbation, $t$ is time, $\rho$ is air density, $U$ is total mean wind speed, $A(x, y, z)$ is the leaf-area density (LAD), and $C_d$ is the unit LAD form drag coefficient. The last term in each of Eqs. (2), (3), and (4) is the parameterized drag force exerted by the shelterbelt following Thom (1975) and Wilson and Shaw (1977). Several investigators used this method to successfully simulate forest and crop flows (Wilson and Shaw 1977; Wilson 1985, 1988; Wilson et al. 1990; Yamada 1982; Meyers and Paw U 1986; Naot and Mahrer 1991; Li et al. 1989; Miller et al. 1991).

The drag force within the shelter exists in all three directions for oblique flow, and the work $W_F$ done by the total drag force may be obtained by integrating along the flow path $S$ through the shelterbelt:

$$W_F = \int_{S=-\infty}^{\infty} C_d A(x, y, z)(u^2 + v^2 + w^2)^{1/2} dS$$

$$dS^2 = dx^2 + dy^2 + dz^2. \quad (5)$$

For normal flow through an infinitely long and horizontally uniform shelterbelt, horizontal wind direction does not change, and $v \equiv 0$ (Wang and Takle 1995). If the vertical component of the drag force is neglected, the drag force is nonzero only in the $x$ direction, and the resistance coefficient or pressure-loss coefficient may be approximated by the method used for a fence (Wilson 1985)

$$k_r = \int_{-\infty}^{\infty} C_d A dx. \quad (6)$$

Under oblique winds, $dS \neq dx$, so $k_r$ no longer represents the actual pressure-loss coefficient or resistance coefficient; however, it still gives an estimate of shelterbelt density and may be considered as a product of $C_d$ and total leaf area in a volume of unit height, unit length, and shelterbelt width. We assume that the shelterbelt has uniform LAD and width of $1H$ ($H$ is the height of the shelterbelt), so $C_d A = k_r/H$. We take $k_r$ = 0.25, 0.5, 2.0, 2.5, and 3.0, which, according to Hoerner's (1965) empirical formula (Wilson 1985, 1988), correspond to estimated porosities of 88%, 75%, 50%, 46%, and 43%, respectively, for a square bar lattice planar fence. Actual drag forces exist in all three directions and are calculated according to Eqs. (2)–(4) by iteration.

Equations (2), (3), and (4) of mean motion include turbulent stress terms for which we must apply one of the boundary layer turbulent closure schemes. Wilson (1985) evaluated several turbulent closure schemes in his numerical study of flow past windbreaks and concluded that first-order closure models gave only slightly less satisfactory results than a second-order closure scheme. Even a very simple eddy viscosity $K_0$ model given by $K_0 = \kappa u_{*0} z$, where $\kappa$ is the von Kármán constant and $u_{*0}$ is the far upstream friction velocity, gave reasonable results in the near wake. Wilson (1985) explained this as a consequence of dominance of pressure gradients and relative unimportance of stress gradients near the shelterbelt. We tested the sensitivity of an hierarchy of turbulence closure $E$–$l$ schemes proposed by Mellor and Yamada (Mellor and Yamada 1974, 1982; Yamada and Mellor 1975; Yamada 1982), and also found that shelterbelt flow is rather insensitive to turbulence closure schemes. For this study, we select an $E$–$l$ turbulence closure scheme that solves prognostic equations only for turbulence kinetic energy (TKE) and master length scale (Yamada 1982). We use the Einstein summation notation to express the turbulence equations more concisely. The correlations of velocity fluctuations (Reynolds stress) may be expressed as

$$-\overline{u_i' u_j'} = K_m\left(\frac{\partial u_i}{\partial x_j} + \frac{\partial u_j}{\partial x_i}\right) - \frac{2}{3}E\delta_{ij}; \quad i = 1, 2, 3, \quad (7)$$

where $l$ is the mixing length (master length) and $E$ is TKE. Following Yamada (1982), the TKE and $l$ (weighted by TKE) can be predicted by

$$\frac{\partial E}{\partial t} = -u_i\frac{\partial E}{\partial x_i} + \frac{\partial}{\partial x_i}\left(K_E\frac{\partial E}{\partial x_i}\right) - \overline{u_i' u_j'}\frac{\partial u_i}{\partial x_j} - c_2\frac{E^{3/2}}{l} + C_d A U^3 \quad (8)$$

$$\frac{\partial El}{\partial t} = -u_i\frac{\partial El}{\partial x_i} + \frac{\partial}{\partial x_i}\left(K_E\frac{\partial El}{\partial x_i}\right) - c_3\overline{l u_i' u_j'}\frac{\partial u_i}{\partial x_j} + -c_4 E^{3/2}\left[1 + c_5\left(\frac{l}{kz}\right)^2\right] + C_d A l U^3, \quad (9)$$

where the turbulent exchange coefficients for TKE and momentum, respectively, are given by

$$K_E = c_6 l E^{1/2}, \tag{10}$$

$$K_m = c_1 l E^{1/2}, \tag{11}$$

and $c_1$–$c_6$ are constants determined from laboratory experiments (Mellor and Yamada 1982; Yamada 1982). We have used this model to simulate the aerodynamic field for flow normal to a shelterbelt, and the results were in a good agreement with observations (Wang and Takle 1995).

We assume that the shelter is infinitely long and therefore the gradients of all physical variables in the $y$ direction are zero. The model computational domain is from $30H$ upstream to $50H$ downstream of the shelterbelt in the horizontal direction and from the ground to $8H$ in the vertical direction. The model top should be kept low enough to neglect Coriolis effects and high enough to minimize effects of the upper boundary on the sheltered zone. As discussed in Wang and Takle (1995), a model top of $8H$ was determined to be a satisfactory compromise. We use 81 levels in the vertical with intervals of $0.1H$ and 161 grid points in the horizontal with intervals of $0.5H$. In tests of sensitivity, horizontal intervals of $0.1H$ and $0.5H$ showed no obvious differences in the simulated results.

At the outflow boundary, normal derivatives of all physical variables ($u$, $v$, $w$, $p$, $E$, and $El$) are set to zero. At the top boundary, $w = 0$, and

$$\frac{\partial El}{\partial z} = \kappa E; \quad K_E \frac{\partial E}{\partial z} = 0; \quad \frac{\partial p}{\partial z} = 0. \tag{12}$$

At the lower boundary, a no-slip condition is imposed for wind; that is, $u = v = w = 0$, and

$$E = c_2^{-2/3} u_*^2; \quad El = \kappa z_0 E; \quad \frac{\partial p}{\partial z} = 0. \tag{13}$$

The turbulence characteristics within the shelter are calculated from Eqs. (8) and (9), which have relatively large contributions from vegetation drag (last term in each equation), and create a new balance of turbulent conditions through these two equations.

We apply a finite differencing method to discretize Eqs. (1)–(4), (8), and (9) into a set of algebraic equations with tridiagonal matrices. The modified Crank–Nicholson scheme with weight $\beta = 0.75$ is used for the flux terms, centered differencing for pressure, upstream differencing for advection terms, and forward differencing in time. The alternating direction implicit method is used to solve these equations in the vertical and horizontal directions, respectively. Gradients of dynamic pressure perturbation are dropped from the horizontal and vertical momentum equations, and auxiliary velocity fields $u^{\text{aux}}$, $v^{\text{aux}}$, and $w^{\text{aux}}$ are computed based on Chorin's (1968) scheme. Results are substituted into the following equations:

$$u^{n+1} = u^{\text{aux}} - \frac{\Delta t}{\rho} \frac{\partial p}{\partial x} \tag{14}$$

$$v^{n+1} = v^{\text{aux}} \tag{15}$$

$$w^{n+1} = w^{\text{aux}} - \frac{\Delta t}{\rho} \frac{\partial p}{\partial z}. \tag{16}$$

We have assumed the shelterbelt is horizontally uniform and infinitely long, and therefore the pressure gradient in the $y$ direction is zero. Calculation of divergence gives

$$\frac{\partial u^{n+1}}{\partial x} + \frac{\partial w^{n+1}}{\partial z} = \frac{\partial u^{\text{aux}}}{\partial x} + \frac{\partial w^{\text{aux}}}{\partial z} - \frac{\Delta t}{\rho}\left(\frac{\partial^2}{\partial x^2} + \frac{\partial^2}{\partial z^2}\right) p. \tag{17}$$

The auxiliary velocity fields are not necessarily mass consistent, but $u^{n+1}$, $v^{n+1}$, and $w^{n+1}$ must satisfy the continuity equation. Therefore, Eq. (17) becomes

$$\left(\frac{\partial^2}{\partial x^2} + \frac{\partial^2}{\partial z^2}\right)\frac{p}{\rho} = \frac{1}{\Delta t}\left(\frac{\partial u^{\text{aux}}}{\partial x} + \frac{\partial w^{\text{aux}}}{\partial z}\right). \tag{18}$$

We solve this dynamic pressure equation by the SOR method with the relaxation factor taken to be 1.75 and the successive convergence criterion set to $|\delta p_{\max}| < 10^{-4}\ \text{m}^2\ \text{s}^{-2}$. After computing dynamic pressure, we correct the velocity fields by Eqs. (14) and (16) to obtain the $n + 1$ step velocity field.

We first ignore the shelterbelt, assume that the surface is horizontally homogeneous, and compute the initial velocity, TKE, and mixing length profiles with a one-dimensional version of the model with a prescribed wind speed at the model top boundary. The initial vertical velocity is set to zero. The resulting profile of horizontal wind speed, which is nearly logarithmic, is used as the inflow condition at the upwind boundary.

We use the time-dependent model to obtain stationary solutions. When differences of mean and turbulent kinetic energy between successive 1-h model integrations are less than control levels (in this paper, 0.01%), the computed results are taken to be steady state.

## 3. Analysis and comparisons of results

### *a. Numerical results*

We define the incident angle $\alpha$ as an angle between the undisturbed wind direction and the normal line ($x$ axis) of the shelterbelt, and the local wind angle $\gamma$ as the angle between local wind direction and the $x$ axis. We calculated flow fields for 19 incident angles ranging from 0° to 90° in 5° intervals for a shelterbelt with porosity of 50%. Figure 1 shows the distributions of horizontal wind vector. Only when the upstream undisturbed wind direction is either parallel ($\alpha$ = 90°)

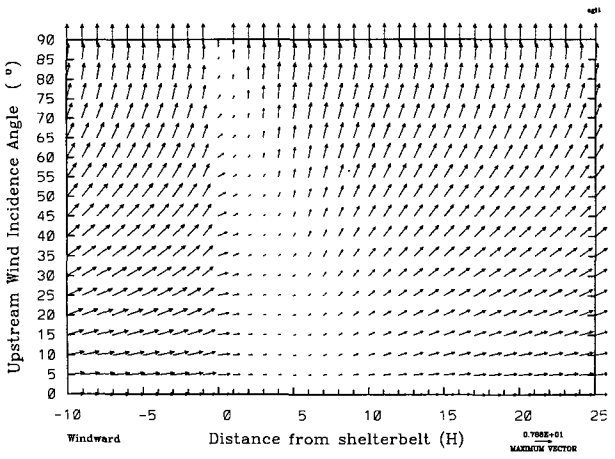


FIG. 1. Wind vectors for airflow through a shelterbelt with porosity of 50% at $z = 0.1H$ with wind incident angles of $\alpha = 0°$–$90°$.

or normal ($\alpha = 0°$) to the shelterbelt does the approaching airflow pass the shelterbelt in a straight horizontal line. When the approach flow is oblique to the shelterbelt, the wind direction near the shelterbelt departs from the incident wind direction.

Figure 2, which shows the distribution of local wind angle $\gamma$ along the $x$ axis, reveals three wind direction shift zones that have distinctive characteristics. The approaching air rotates toward the direction parallel to the shelterbelt, with a maximum departure just in front of the barrier; this is followed by an abrupt rotation in the opposite direction passing through the incident angle to a maximum departure in the opposite direction just behind the shelterbelt. Beyond this point, the wind rotates back toward the incident angle at a few $H$ downstream. Rotation continues past the incident angle, the wind becoming more parallel to the shelterbelt, and produces a maximum shift at a distance of $2$–$12H$. Further leeward, the wind slowly rotates back to the undisturbed angle.

The local wind direction twice passes through the incident direction, the two zero-departure points being in front of the shelterbelt and in the near lee. The changes of wind direction may be divided into three zones separated by these two points. We define the upwind zone where the attack angle is greater than the incident angle as the F (front) zone. The zone within and just behind the shelterbelt where the wind direction becomes less oblique (less than the incident angle), we define as the B (behind) zone. The region beyond the B zone, where the wind direction becomes more parallel to the shelterbelt (greater than incident angle), we define as the W (wake) zone.

The dependence of wind rotation on height is shown by horizontal profiles at different heights for each incident angle in Fig. 2. The wind direction shift decreases with height for all incident angles and for all three zones. However, the change of wind rotation with height is different for different horizontal locations. In the B zone, within $1H$ immediately behind the shelter, wind rotation slowly decreases with height below $z = 0.7H$, but the change with height is rapid in other places in this zone. In the W zone, the wind rotation decreases with height in the mid lee, but slightly increases with height in the far lee. The wind rotation change with height is larger for small incident angles, the rates of the maximum shift at $z = 0.1$ being about 3 times the maximum shift at $z = 0.3H$ for $\alpha = 15°$, but only twice as much for $\alpha = 75°$. In the F zone, the decrease of wind rotation with height under $z = 0.7H$ is slower than that in either B or W zones.

Figures 3a–c show the distributions of the maximum wind shift angle versus incident wind angle for the F, B, and W zones, respectively. As shown in Fig. 3a, the maximum local wind direction shift angle in the F zone occurs for incident angles between 30° and 40°, and the maximum decreases with increasing height. The wind direction shift at $z = 0.6H$ is about half of that at $z = 0.1H$, and above $1.5H$ the perturbation is rather weak. From Fig. 3b, we can see that the maximum shift in wind direction in the B zone occurs for a wind approach angle between $\alpha = 60°$ and 70°. The maximum shift decreases rapidly with increasing height near the surface, decreases slowly with height between $0.3H$ and $0.8H$, decreases rapidly again near $z = 1.0H$, and then slowly above the top of the shelter. For the W zone, as shown in Fig. 3c, the maximum wind vector rotation occurs at $\alpha = 40°$ near the surface, and decreases rapidly with increasing height. At higher levels the peak of the curve is less well defined but occurs at larger incident angles.

For convenience, we define the horizontal distance between two zero-departure points as the range $R_B$ of the B zone. We define the horizontal distance between first zero-departure point and the point where wind direction shift at $z = 0.1H$ is larger than 1° far upwind as the range $R_F$ of the F zone. Finally, we define the horizontal distance between the second zero-departure point and the point in the far lee where wind direction shift at $z = 0.1H$ is larger than 1° as the range $R_W$ of the W zone.

The ranges of the three zones also change with height, as shown in Fig. 2. The location of the near-shelter end of the W zone moves away from the shelterbelt with increasing height. For an incident angle of 45° we can see that the range of the B zone increases from $3.3H$ at $z = 0.1H$ to $7.5H$ at the height of the shelterbelt top. Correspondingly, the near-shelter edge of the W zone moves $4.2H$ farther downstream from $z = 0.1H$ to $z = 1.0H$, and the location of the maximum wind direction shift in the W zone moves from $5.5H$ at $z = 0.1H$ to $z = 20.0H$ at $z = 1.0H$.

The range of the F zone increases with incident angle from $0H$ at $\alpha = 0°$ to a maximum of $11H$ at $\alpha = 45°$, and then decreases with further increase of incident angle to $0H$ at $\alpha = 90°$ (Fig. 2). For the W zone, the

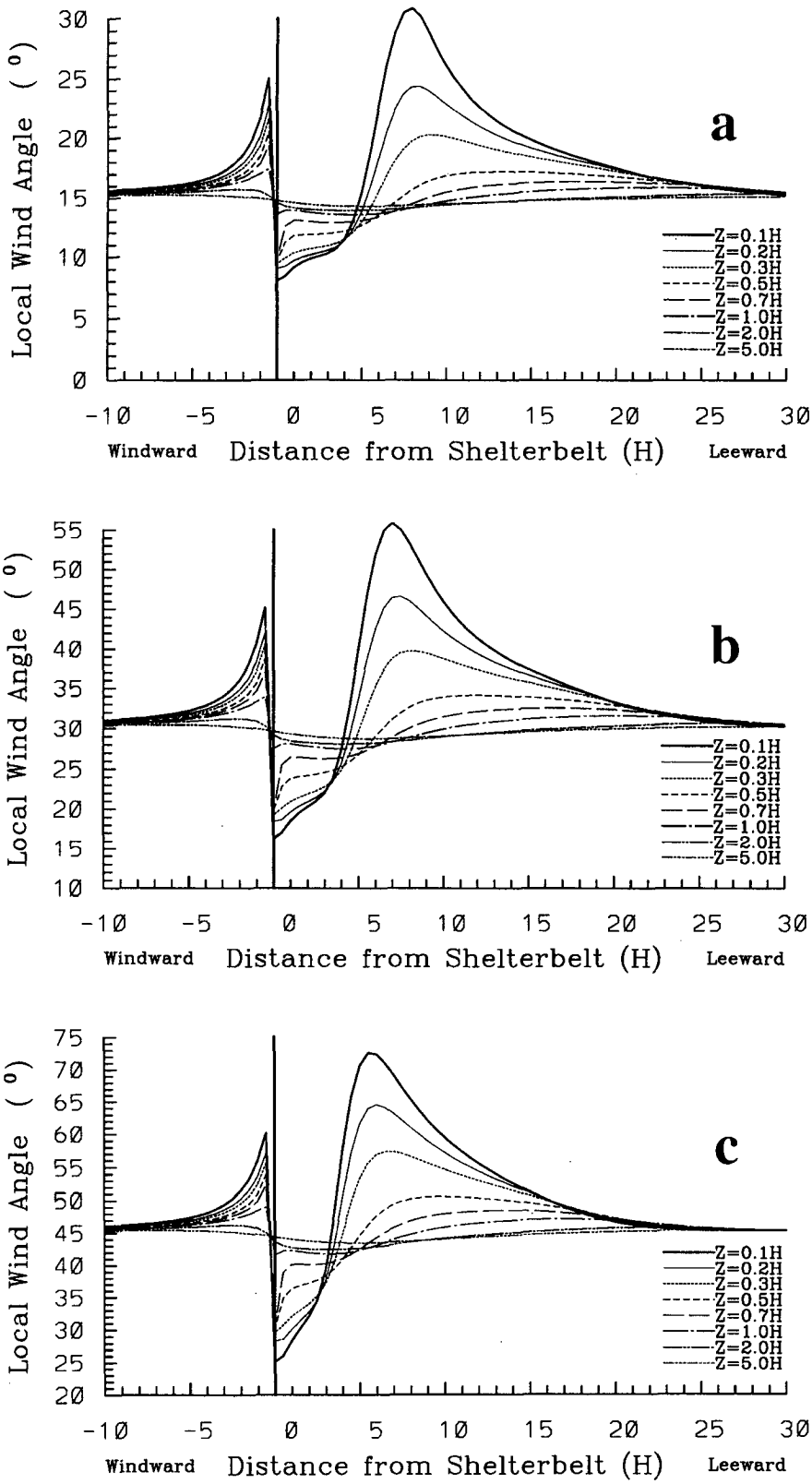


FIG. 2. Horizontal distributions at various heights of local wind angle for airflow through a shelterbelt with porosity of 50% for wind incident angle (a) $\alpha = 15°$, (b) $\alpha = 30°$, (c) $\alpha = 45°$, (d) $\alpha = 60°$, and (e) $\alpha = 75°$.

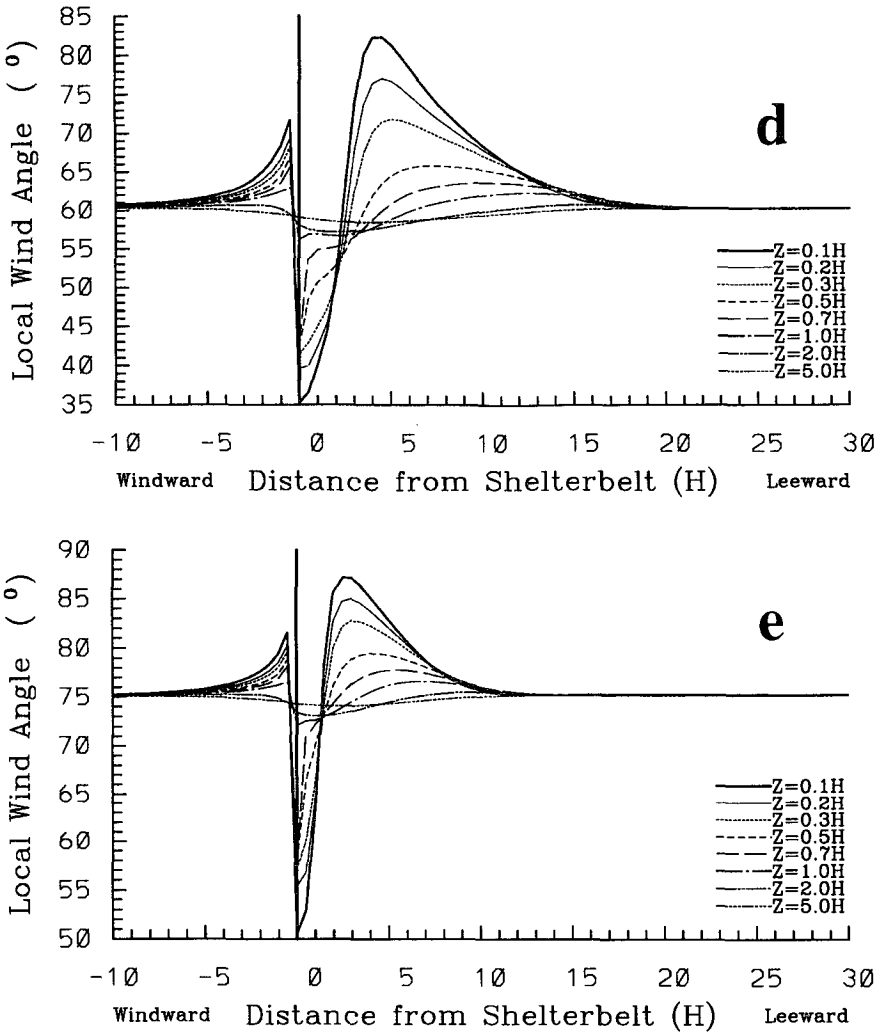


FIG. 2. (*Continued*)

change of the range with incident angle is analogous to the F zone, but the maximum range occurs between $\alpha = 15°$ and 30°. The range of the B zone is maximum between $\alpha = 0°$ and 15° and decreases with increasing incident angle from $5.0H$ at $\alpha = 15°$ to $0H$ at $\alpha = 90°$. The maximum wind rotation does not occur at the same incident angle as the maximum horizontal range for any of the zones.

We also calculated the influence of porosity on shelterbelt-induced wind vector rotation for different incident angles. As listed in Table 1, in both the B and F zones, the maximum wind shift increases more slowly with decreasing porosity than in the W zone for $\alpha = 30°$. Although the porosity decreases only from 50% to 43%, which sometimes is considered to be the range of optimal porosity (van Eimern et al. 1964; Heisler and DeWalle 1988), the wind rotation in the W zone increases from 26° to 49° for $\alpha = 30°$. We can expect that wind rotation increases more rapidly with a further decrease of porosity and may exceed 180° when the recirculation bubble forms (Wang and Takle 1995). For an incident angle of 60°, the wind vector rotation in the W zone is less dependent on porosity, in the B zone it is more dependent, and in front of the shelter, it is nearly unchanged. For an incident angle of 45°, the situation is intermediate. In summary, with decreasing porosity, the wind direction shift increases in both the B zone and the W zone; in the F zone, the wind direction shift increases first rapidly but then more slowly for porosity larger than 50% (figures omitted). The net result of this is that the W zone has the smallest maximum wind shift for porous shelters but the largest maximum for dense shelters.

With decreasing porosity, the range of the F zone increases, but the range of the B zone decreases (Table 2). For the W zone, the range reaches its maximum at intermediate density (shelterbelt porosity of 50%),

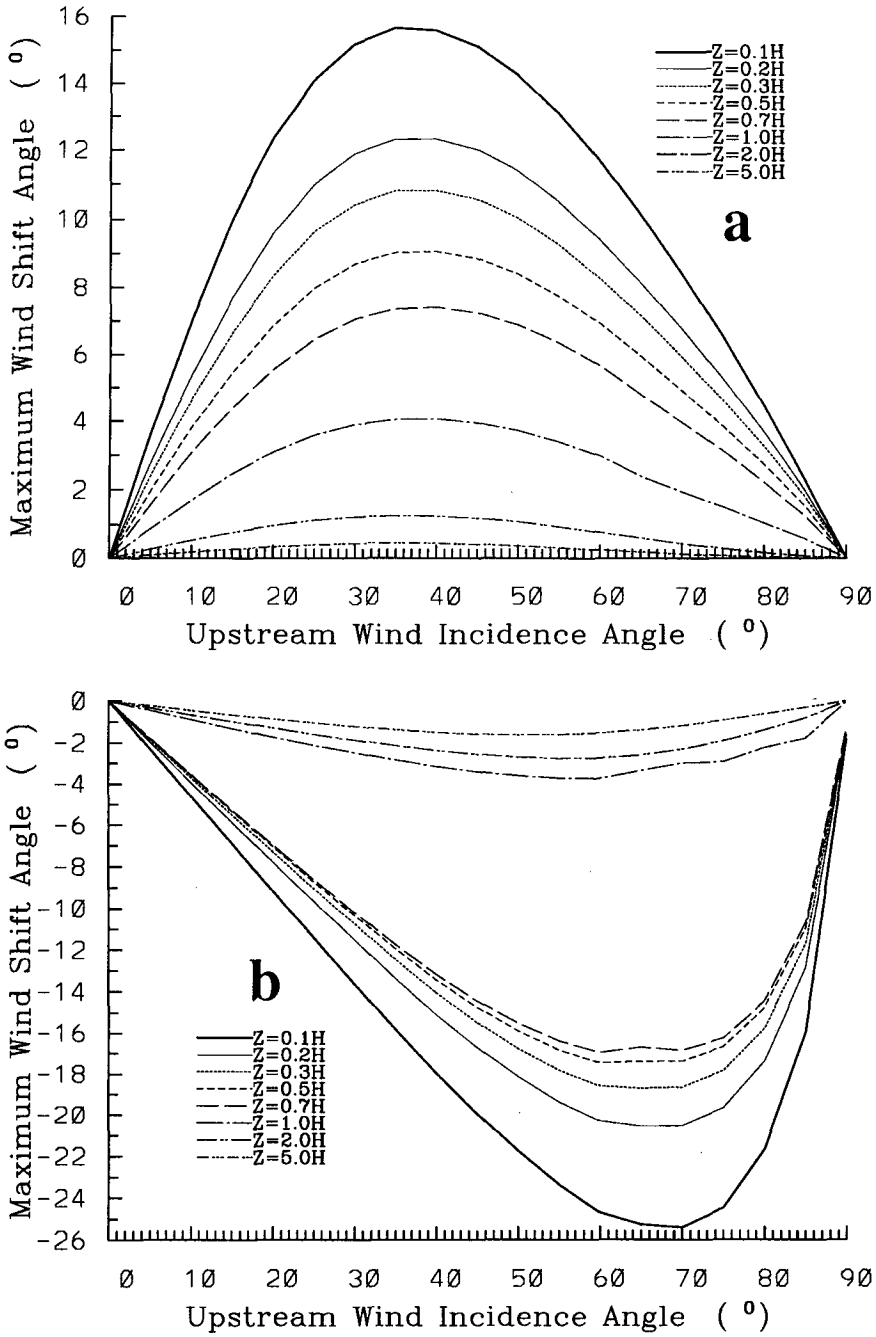


FIG. 3. Relationships between maximum wind-shift angle and upstream undisturbed wind incident angle near a shelterbelt with porosity of 50% in (a) F, (b) B, and (c) W zones.

and the location of maximum wind shift moves farther downstream with increasing porosity.

### *b. Comparison with observations*

Nord (1991) reported quantitative observations of the effect of shelterbelts on wind direction. Three-component anemometers equipped with light propellers of the Gill type were used to measure wind velocity under neutral stability at 2 m at several sites along a line perpendicular to a multiple-row shelterbelt with west-northwest–east-southeast orientation situated in the south of Sweden. This belt was composed of birches and spruce with an average height of 12 m, length of 100 m, and width of 20 m. The porosity, determined by matching the horizontal wind profile between the

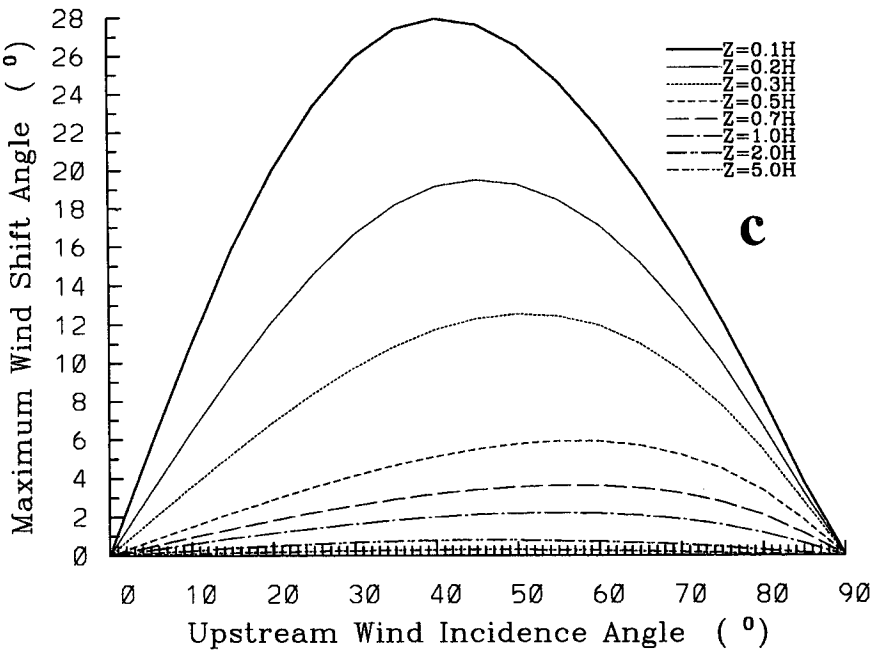


FIG. 3. (*Continued*)

wind tunnel model and the full-scale field shelterbelt, was estimated to be 0.55 in the upper part and 0.23 in the lower part.

Distributions of local wind direction $\gamma$ versus airflow approach direction $\alpha$ in the F, B, and W zones, shown in Figs. 4a–c, respectively, are simulated for the conditions of Nord's (1991) field observations. The local wind angle in the F zone (Fig. 4a) is always greater than $\alpha$. Although Nord (1991) did not give detailed data for the F zone, our simulated maximum wind direction shift of 18° is within his observed range of 15°–20°. Figure 4b shows that our simulations for the B zone compared well to the observed data taken from Fig. 13 of Nord (1991). Our calculations for the W zone are compared to measurements taken from Fig. 14 of Nord (1991). As shown in Fig. 4c, the simulated results agree with observations for $\alpha < 40°$; for higher incident angles, Nord's data show that the wind direction shift decreases faster than our simulation shows. In our simulation, we have assumed that the shelterbelt is infinitely long, but in Nord's (1991) field observations, the shelterbelt had a height of 12 m and was only 100 m long. According to Naegeli (cited by van Eimern et al. 1964), the ratio of length to height of a shelterbelt must be at least 11.5 if the wind conditions of an infinitely long belt are to be achieved for a line perpendicular to its center and airflow at a right angle; for oblique flow, the ratio must be much larger than 11.5. In the region where edge effects are important, the local wind direction will be expected to be closer to the angle of the approach flow. Nord's (1991) data likely include edge effects of such a short shelterbelt at such large angles. Considering this factor, we can reasonably say that our model also gives good predictions in the W zone.

Nord's (1991) field observations showed that the wind in front of a dense shelterbelt was deflected about as much in winter as in summer, but behind the same belt and in the far lee, the greater porosity of a leafless belt in the winter made the wind shift considerably less

TABLE 1. Maximum wind rotation (°) for different incident angles $\alpha$, shelter porosity, and shelterbelt zones.

| Porosity (%) | $\alpha$ = 30° | | | $\alpha$ = 45° | | | $\alpha$ = 60° | | |
|---|---|---|---|---|---|---|---|---|---|
| | F | B | W | F | B | W | F | B | W |
| 88 | 4 | −5 | 1 | 5 | −7 | 2 | 5 | −9 | 2 |
| 75 | 7 | −6 | 2 | 9 | −9 | 4 | 7 | −12 | 4 |
| 50 | 17 | −14 | 26 | 16 | −20 | 28 | 11 | −25 | 22 |
| 46 | 18 | −15 | 39 | 17 | −22 | 36 | 13 | −27 | 27 |
| 43 | 18 | −16 | 49 | 17 | −24 | 44 | 14 | −30 | 29 |

TABLE 2. Horizontal ranges of the three shelterbelt zones and location of maximum wind shift in the W zone for different shelterbelt porosities.

| Porosity (%) | $R_F$ ($H$) | $R_B$ ($H$) | $R_W$ ($H$) | Location ($H$) of max shift in W |
|---|---|---|---|---|
| 88 | 4.0 | 6.0 | 18.0 | 12.5 |
| 75 | 6.0 | 5.5 | 19.5 | 11.0 |
| 50 | 10.0 | 3.3 | 22.0 | 6.0 |
| 46 | 11.0 | 3.0 | 21.5 | 5.5 |
| 43 | 12.0 | 2.8 | 21.0 | 5.0 |

than in summer. These results are in agreement with our calculations of the influence of porosity as shown in Table 1. Nord (1991) also reported that a single row of poplars (mean porosity of 0.64) produced a wind shift smaller and farther downstream compared to effects of a dense multiple-row belt (mean porosity of 0.39). These results agree with our calculations of the dependence of range on porosity as summarized in Table 2.

## 4. Summary and discussion

Our interest in wind rotation induced by shelterbelts is driven by both fundamental and practical considerations. Wind rotation and its change with height imply that atmospheric surface boundary layer (SBL) theory, which is based on uniform wind direction in the SBL (neglecting the Coriolis force), is not strictly applicable and that shear of wind direction as well as speed can be a source of turbulence. Unfortunately, most previous observations have not provided measurements of wind direction, and fluxes derived from wind measurements without regard to wind direction in oblique flows is questionable. Observations of wind shift made by Nord (1991) are at only one level near ground, and to our knowledge no other detailed quantitative wind direction data are available. Our simulations give the spatial variation and the range of wind rotation and their relationships to shelterbelt porosity and incident angle.

Almost all previous theoretical and numerical studies have addressed only flow normal to the shelterbelt, with little attention given to their relevance for the more commonly occurring oblique flows. For convenience of analysis, it is usually assumed that the trajectory of airflow through the shelterbelt is a straight horizontal line, so that the results for oblique flows may be projected onto the normal line of the shelterbelt by multiplying by $\cos(\alpha)$. Our simulated results show that wind direction may change by as much as 50° for a medium-dense shelterbelt, which raises questions about the validity of the cosine projection method. Another convenient simplification in analyzing sheltering effects for oblique flows is that the shelterbelt affects only the normal component of wind and does not change the parallel component. To examine the validity of these simplified views we summarize the basic force balances near and within the shelter.

The drag force produces a pressure perturbation that contributes to the balance of forces for flow approaching the shelter. The characteristics of the three wind rotation zones and their changes with shelterbelt porosity, incident angle, and height are closely related to the distribution of perturbed pressure. A positive pressure perturbation is established on the windward side, and a negative pressure perturbation is created in the lee. Perturbed pressure fields for three approach angles are shown in Figs. 5a–c, where the pressure perturbation is normalized by the mean kinetic energy of the approach wind at $z = 1.0H$. The assumption of an infinitely long shelterbelt means that air must flow through or over the shelter (not around), and that the resulting gradients of pressure are all normal to the belt. The windward positive pressure perturbation sets up a force normal to the shelter in the windward direction, and the negative pressure perturbation in the lee creates a leeward-directed pressure gradient normal to the belt that also gives a force directed windward. Therefore, the pressure gradient tends to reduce the component of the wind perpendicular to the shelterbelt on both leeward and windward sides, thereby creating the F and W zones. The large pressure gradient across the shelterbelt rotates the wind more normal to the shelter as it passes through, thereby creating the B zone within the shelterbelt.

From Fig. 5, we also can see that the pressure gradient is relatively weak in the near lee compared to the windward side, especially within a few $H$ downstream. This causes the wind vector behind the shelterbelt to recover to the undisturbed angle quite slowly, thereby retaining its less oblique direction several $H$ behind the shelterbelt and stretching the range of the B zone to beyond the shelter.

The near-lee weak gradient of perturbed pressure in Fig. 5a arises from interactions of flow and pressure. The leeward wind speed reaches its minimum at several $H$ downstream from the shelterbelt. In this region, the convergence of the wind field is associated with a positive additional pressure [see Eq. (18)], which produces a very weak pressure gradient within a few $H$ in the lee. However, beyond the point of minimum wind speed, negative additional pressure generated by divergence of the wind field leads to a larger pressure gradient that makes the wind vector rotate back rapidly in the B zone and produces a larger rotation in the W zone, as shown in Figs. 2a–e. For increased angles of incidence (Figs. 5b,c), both value and horizontal range of the pressure perturbation decrease, especially for the range of weak pressure gradient behind the shelterbelt. The resulting horizontal range of the B zone decreases with increasing incident angle.

Advection also contributes to rotation of the wind vector, which is demonstrated in Figs. 6a and 6b by

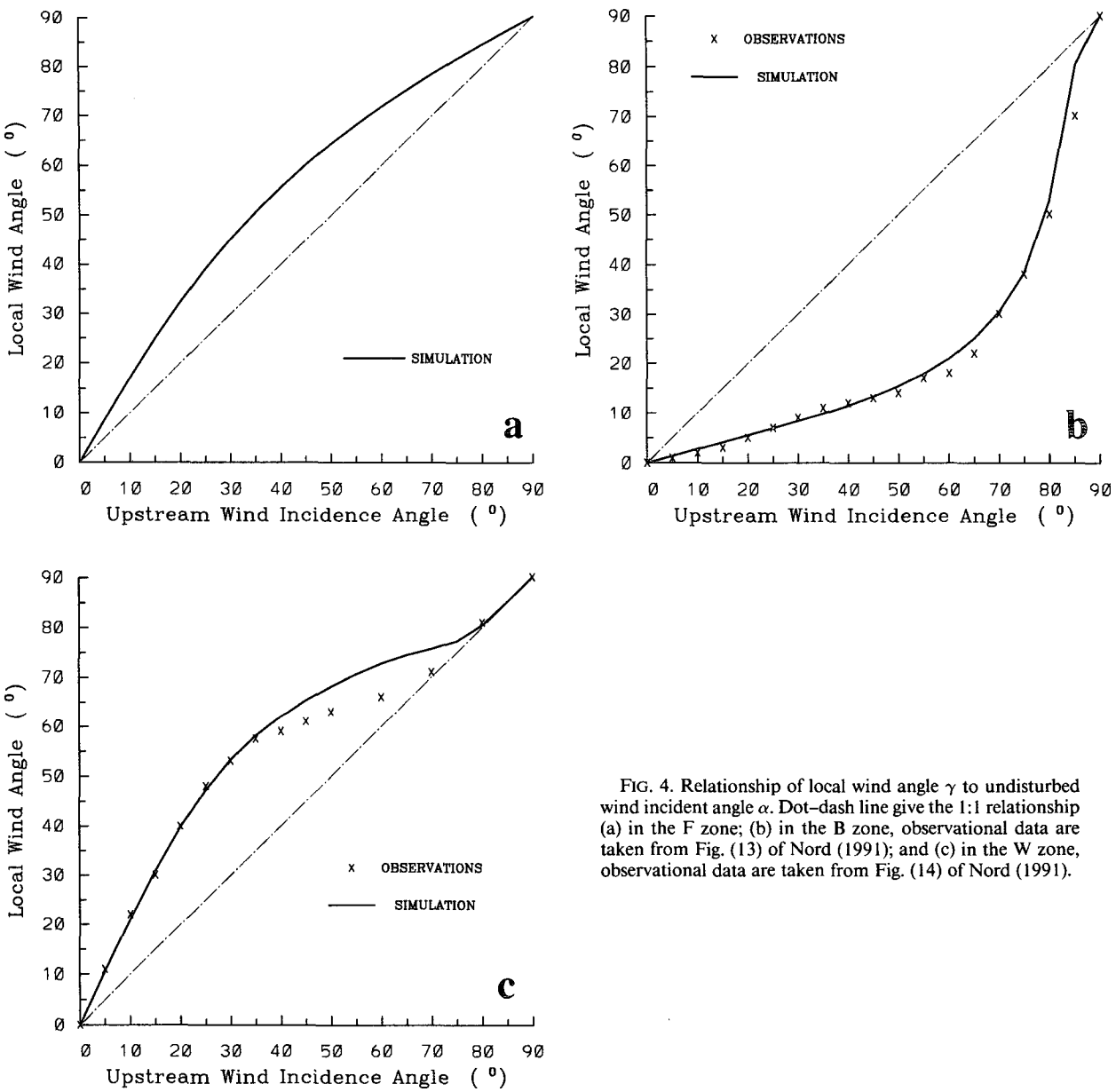


FIG. 4. Relationship of local wind angle $\gamma$ to undisturbed wind incident angle $\alpha$. Dot–dash line give the 1:1 relationship (a) in the F zone; (b) in the B zone, observational data are taken from Fig. (13) of Nord (1991); and (c) in the W zone, observational data are taken from Fig. (14) of Nord (1991).

the distributions of wind speed components normal and parallel to a shelter of porosity 50% at a height of $0.1H$. From Fig. 6a, we can see that $u$ decreases both windward and leeward, with minima of $u$ immediately in front of the belt and within a few $H$ leeward. Within the shelterbelt, $u$ increases due to acceleration by the large pressure gradient across the belt. As the flow becomes more oblique to the shelter, the windward reduction of $u$ increases, the leeward range of the $u$-reduction zone is diminished, the location of the leeward minimum $u$ moves toward the belt, and $u$ increases more within the shelter.

An unanticipated result for us was that, as shown in Fig. 6b, the $v$ component also changes dramatically with $x$. In the lee, the change of $v$ with $x$ is similar to that of $u$, but the horizontal range of the $v$-reduction zone is shorter, and in the mid lee, $v$ is larger than the undisturbed $v_0$. On the windward side, $v$ increases to as much as 120% of $v_0$, in contrast to $u$, which decreases in approaching the belt.

With increasing height, the minimum $u$ first increases slowly from 15% at $z = 0.1H$ to 35% at $z = 0.8H$, but rapidly increases near the shelterbelt top to 85% at $z = 1.1H$. Although the minimum $v$ hardly changes with $z$ under $z = 0.8H$, the locations of minimum $v$ move toward the belt and are immediately behind the belt at $z = 0.8H$ for all incident angles. The

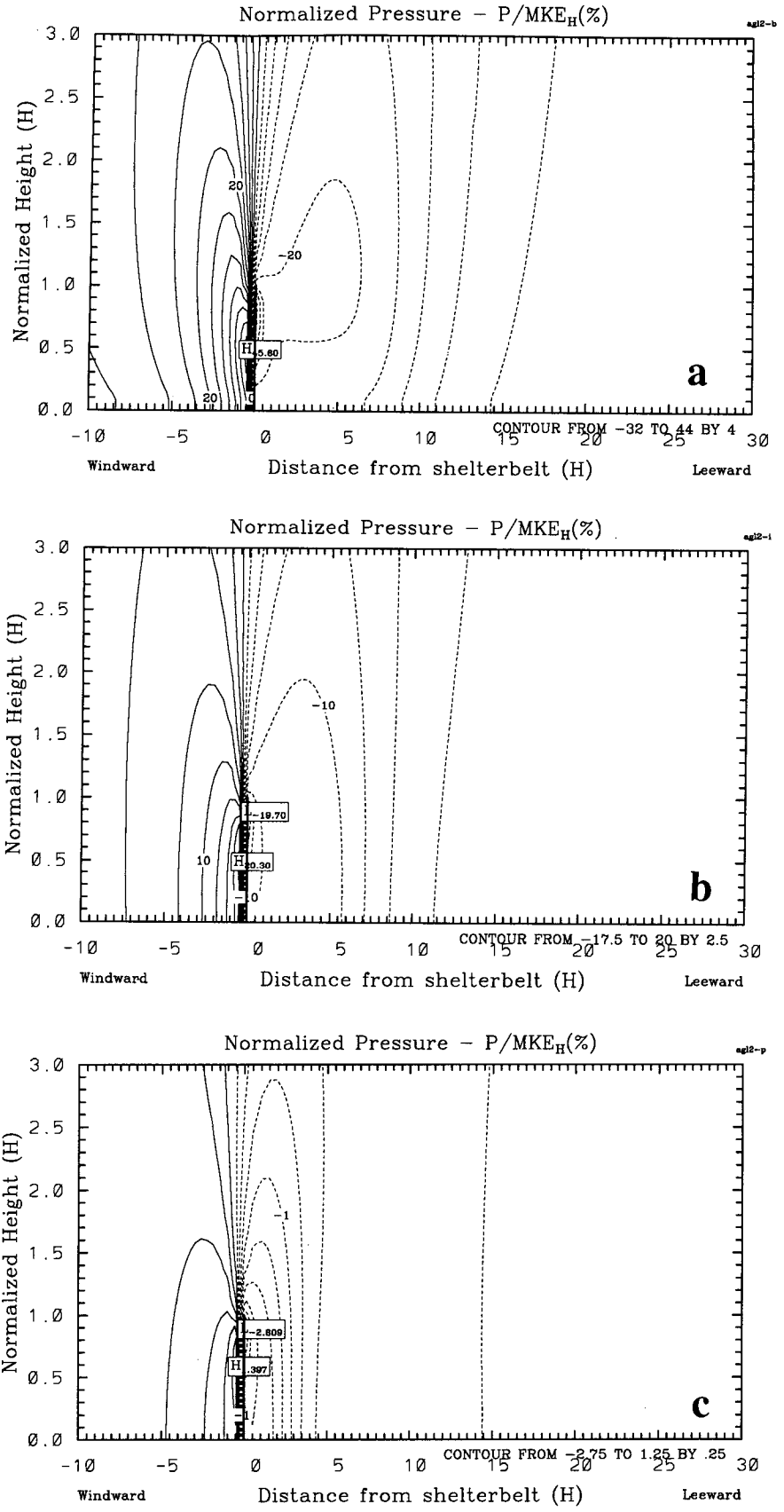


FIG. 5. Pressure perturbation for airflow through a shelterbelt with porosity of 50% for incident angle (a) $\alpha = 10°$, (b) $\alpha = 45°$, and (c) $\alpha = 80°$.

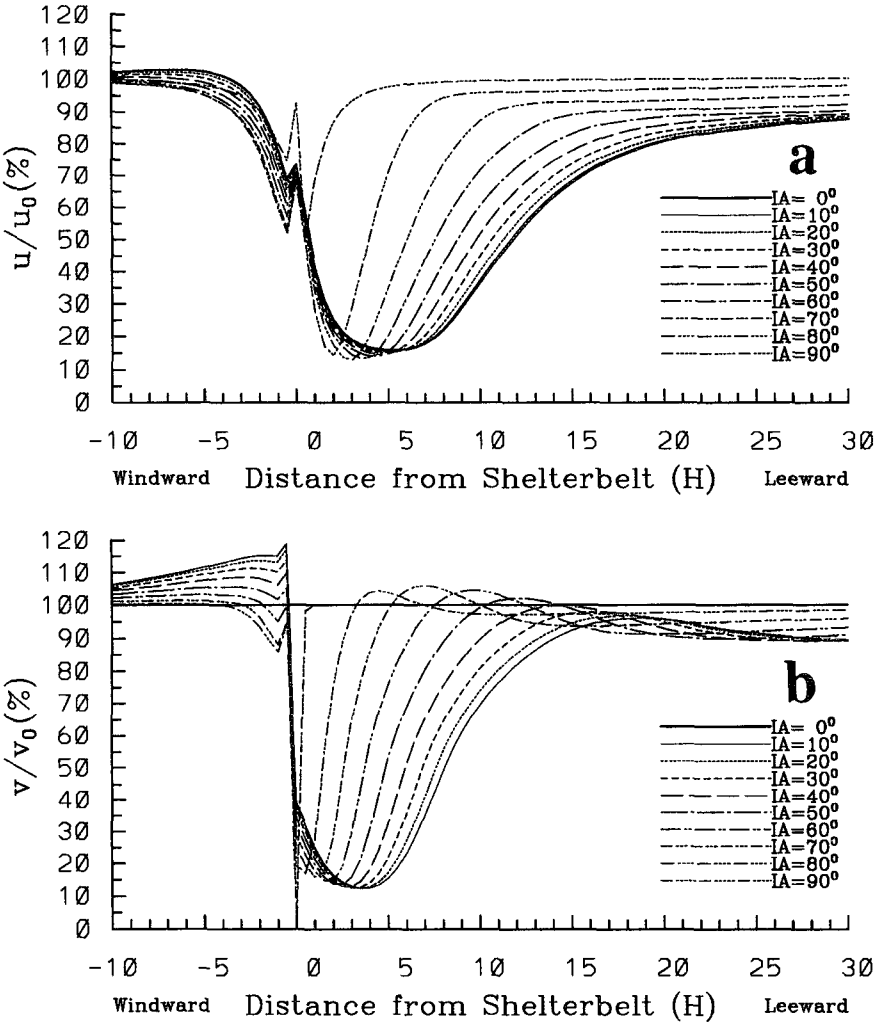


FIG. 6. Horizontal distribution of wind components across the shelterbelt at $z = 0.1H$, (a) normal component $u$, (b) parallel component $v$.

$v$ rapidly recovers to 100% (undisturbed value) near the shelterbelt top (figure omitted).

Mechanisms responsible for the change of $v$ outside the shelter need clarification. For an infinitely long shelterbelt and steady-state conditions, Eq. (3) is simplified due to loss of the tendency term (left-hand side), the three terms having $y$ gradients, and the drag term that is nonzero only within the shelter. This leaves advection and turbulent exchange in the $x$ and $z$ directions as possible mechanisms for the anomalous increase in $v$. Because vertical gradients of $v$ and $v'w'$ are likely larger than horizontal gradients of $v$ and $u'v'$, $v$ likely increases due to downward transport by these two processes.

## 5. Conclusions

Aerodynamic drag of shelterbelts is the root cause of any shelter effect, including wind rotation. For oblique flow, spatial changes of pressure perturbation generated by the shelter drag force, additional pressure perturbation generated by convergence and divergence of the wind field, and mean and turbulent transports of momentum cause wind rotation. However, wind rotation alters the airflow path and hence changes the drag force and pressure perturbation. These, in turn, change mean flows and turbulence and create changes of pressure perturbation and mean and turbulent transports of momentum. These interactions lead to complexities in the determination of sheltering effects that cannot be accurately determined from considering only the normal component of oblique flows. Wind rotation as well as its change with height complicates the calculation of turbulent fluxes and the resulting surface exchanges of heat, momentum, and moisture over crops in the sheltered region.

Observations of the spatial variation of the three-dimensional wind vector are needed for understanding

the sheltering effect for oblique flows. Field testing of our predictions for the regions having large wind vector rotation will determine the level of confidence we can expect for calculations of the turbulence fluxes in regions where wind rotation is large. Refinement of our understanding of the wind vector will allow us to develop a more accurate description of the microclimate in the sheltered region.

*Acknowledgments.* The authors would like to thank two anonymous reviewers for their careful review leading to improvements in the manuscript. This research was supported by USDA/CSRS Grant 93371018954.

## APPENDIX

### Notation

| | |
|---|---|
| overbar ($^-$) | Spatial or temporal averaged value |
| prime ($'$) | Departure of variable from its average value |
| $A$ | Leaf surface-area density |
| B | Zone within and behind the shelterbelt with less oblique wind direction shift |
| $c_i$ | Experimental constants of the turbulent closure scheme (Mellor and Yamada 1982) |
| $C_d$ | Drag coefficient for unit plant leaf-area density (LAD) |
| $E$ | Turbulent kinetic energy (TKE) |
| F | Zone in front of the shelterbelt with more oblique wind-direction shift |
| $H$ | Height of shelterbelt |
| $i, j, k$ | Subscript variables, indicating $x$, $y$, and $z$ directions, respectively, and grid numbers in these three directions |
| $k_r$ | Resistance coefficient or pressure-loss coefficient for planar fences, product of $C_d$ and total leaf area of cubic column of the shelterbelt width, unit height, and unit length |
| $K_0$ | Turbulent exchange coefficient for upstream undisturbed flow |
| $K_m$ | Turbulent exchange coefficient for momentum transport |
| $K_E$ | Turbulent exchange coefficient for TKE transport |
| $l$ | Mixing length of turbulence |
| $m$ | Porosity of shelterbelt |
| MKE | Mean kinetic energy |
| $n$ | Time-step number |
| $R_F$ | Horizontal range of the F zone |
| $p$ | Atmospheric pressure perturbation |
| $R_B$ | Horizontal range of the B zone |
| $R_W$ | Horizontal range of the W zone |
| $S$ | Path of airflow |
| $U$ | Total mean wind speed |
| $u, v, w$ | Mean wind speed components in $x$, $y$, and $z$ directions |
| $u', v', w'$ | Fluctuating wind speed components in $x$, $y$, and $z$ directions |
| $u_i$ | Wind speed in direction $i$, $i = 1, 2, 3$ |
| $u_{*0}$ | Friction velocity for upstream undisturbed flow |
| $u_*$ | Friction velocity |
| $u^{aux}, v^{aux}, w^{aux}$ | The intermediate prediction velocities of $u$, $v$, and $w$ without the pressure perturbation |
| W | Zone leeward of the shelterbelt with more oblique wind direction (wake zone) |
| $W_F$ | Work done by drag force for airflow through shelterbelts |
| $x$ | The horizontal coordinate axis perpendicular to the shelterbelt |
| $y$ | The horizontal coordinate axis along the shelterbelt |
| $z$ | Vertical coordinate |
| $z_0$ | Ground surface roughness length |
| $x_i$ | $i = 1, 2, 3$—three direction coordinates, $x$, $y$, $z$ |
| $\epsilon_{ijk}$ | Einstein summation symbol |
| $\rho$ | Air density |
| $\alpha$ | Upstream undisturbed wind incident angle between wind direction and the normal line to the shelterbelt ($x$ axis) |
| $\beta$ | Weight coefficient in differencing scheme |
| $\gamma$ | Angle between local wind and the normal line to the shelterbelt (between local wind vector and the $x$ axis) |
| $\Delta t$ | Time step of model integration |
| $\kappa$ | von Kármán constant |

## REFERENCES

Brinmann, K., and H. Kaiser, 1955: Maize strips as windbreaks, meteorological investigations and yield. *Z. Acker-u. Pflanzenbau,* **99,** 321–334.

Chorin, A. J., 1968: Numerical solution of the Navier–Stokes equations. *Math. Comp.,* **23,** 341–354.

Counihan, J. J., C. R. Hunt, and P. S. Jackson, 1974: Wakes behind two-dimensional surface obstacles in turbulent boundary layers. *J. Fluid Mech.,* **64,** 529–563.

Hagen, L. J., E. L. Skidmore, P. L. Miller, and J. E. Kipp, 1981: Simulation of effect of wind barriers on airflow. *Trans. ASAE,* **24,** 1002–1008.

Heisler, G. M., and D. R. Dewalle, 1988: Effects of windbreak structure on wind flow. *Agri. Ecosyst. Environ.,* **22/23,** 41–69.

Hoerner, S. F., 1965: *Fluid Dynamic Drag.* Library of Congress Catalog Card Number 64-19666, 60–166.

Kaiser, H., 1959: Die stromung an windschutzstreifen. *Ber. Dtsch. Wetterdienstes,* **7,** 36 pp.

Li, Z., J. D. Lin, and D. R. Miller, 1989: Air flow over and through a forest edge: A steady-state numerical simulation. *Bound.-Layer Meteor.,* **46,** 333–354.

McNaughton, K. G., 1988: Effects of windbreaks on turbulent transport and microclimate. *Agri. Ecosyst. Environ.,* **22/23,** 17–39.

Mellor, G. L., and T. Yamada, 1974: A hierarchy of turbulence closure models for planetary boundary layers. *J. Atmos. Sci.,* **31,** 1791–1806.

——, and ——, 1982: Development of a turbulent closure model for geophysical fluid problems. *Rev. Geophys. Space Sci.*, **20,** 851–875.

Meyers, T., and K. T. Paw, U., 1986: Testing of a higher-order closure model for modeling airflow within and above plant canopies. *Bound.-Layer Meteor.*, **37,** 297–311.

Miller, D. R., J. D. Lin, and Z. N. Lu, 1991: Air flow across an alpine forest clearing: A model and field measurements. *Agri. For. Meteor.*, **56,** 209–225.

Naot, O., and Y. Mahrer, 1991: Two-dimensional microclimate distribution within and above a crop canopy in an arid environment: Modeling and observational studies. *Bound.-Layer Meteor.*, **56,** 223–244.

Nord, M., 1991: Shelter effects of vegetation belts—Results of field measurements. *Bound.-Layer Meteor.*, **54,** 363–385.

Plate, E. J., 1971: The aerodynamics of shelter belts. *Agri. Meteor.*, **8,** 203–222.

Rosenberg, N. J., 1979: Windbreaks for reducing moisture stress. *Modification of Aerial Environment of Plants,* B. J. Barfield and J. F. Gerber, Eds., ASAE, St. Joseph, 394–408.

Taylor, P. A., 1988: Turbulent wakes in the atmospheric boundary layer. *Flow and Transport in the Natural Environment: Advances and Applications,* Steffen, W. L. and O. T. Denmead, Eds., Springer-Verlag, 270–292.

Thom, A. S., 1975: *Vegetation and the Atmosphere.* Vol. 1. Academic Press, 278 pp.

van Eimern, J., R. Karschon, L. A. Razumova, and G. W. Robertson, 1964: Windbreaks and shelterbelts. World Meteorological Organization Tech. Note No. 59, 188 pp.

Wang, H., 1991a: The effects of shelterbelts on the atmospheric turbulent exchange coefficient. *Acta Geogr. Sin.*, **46,** 107–114.

——, 1991b: A numerical simulation of the wind sheltering effects of multiple parallel shelterbelts. *J. Nanjing Univ.*, 481–488.

——, 1992: On methods for the study about the protection effects of shelterbelts. *Promoting Agriculture through the Progress of Science and Technology,* Eastern China Agricultural Association, Jiangsu Sci. and Tech. Press, 369–372.

——, and J. M. Shen, 1989: A two-dimensional numerical study of the wind sheltering effects of shelterbelts. *Acta Meteor. Sin.*, **3,** 498–505.

——, and E. S. Takle, 1995: Boundary-layer flow and turbulence near porous obstacles. Part I: Derivation of a general equation set for a porous medium. *Bound.-Layer Meteor.*, **74,** 73–88.

Wilson, J. D., 1985: Numerical studies of flow through a windbreak. *J. Wind Eng. Ind. Aerodyn.*, **21,** 119–154.

——, 1987: On the choice of a windbreak porosity profile. *Bound.-Layer Meteor.*, **38,** 37–39.

——, 1988: A second-order closure model for flow through vegetation. *Bound.-Layer Meteor.*, **42,** 371–392.

——, G. E. Swaters, and F. Ustina, 1990: A perturbation analysis of turbulent flow through a porous barrier. *Quart. J. Roy. Meteor. Soc.*, **116,** 989–1004.

Wilson, N. R., and R. H. Shaw, 1977: A higher order closure model for canopy flow. *J. Appl. Meteor.*, **16,** 1197–1205.

Yamada, T., 1982: A numerical model study of turbulent airflow in and above a forest canopy. *J. Meteor. Soc. Japan,* **60,** 438–454.

——, and G. L. Mellor, 1975: A simulation of the wangara atmospheric boundary layer data. *J. Atmos. Sci.*, **32,** 2309–2329.